Drying Technology

An International Journal

ISSN: 0737-3937 (Print) 1532-2300 (Online) Journal homepage: http://www.tandfonline.com/loi/ldrt20

Numerical and experimental analysis of the single droplet evaporation in a ultrasonic spray pyrolysis device

Peter Majerič, Rebeka Rudolf, Bernd Friedrich & Primoz Ternik

To cite this article: Peter Majerič, Rebeka Rudolf, Bernd Friedrich & Primoz Ternik (2017): Numerical and experimental analysis of the single droplet evaporation in a ultrasonic spray pyrolysis device, Drying Technology, DOI: 10.1080/07373937.2017.1292520

To link to this article: http://dx.doi.org/10.1080/07373937.2017.1292520

Accepted author version posted online: 23 Feb 2017.

Numerical and Experimental Analysis of the Single Droplet Evaporation in a Ultrasonic Spray Pyrolysis Device

Peter Majerič[1], Rebeka Rudolf[1], Bernd Friedrich[2], Primoz Ternik[3]

[1]Faculty of Mechanical Engineering, Maribor, Slovenia [2]IME Institute of Process Metallurgy and Metal Recycling, RWTH Aachen, Aachen, Germany [3]Ternik Primož- Private Researcher, Bresternica, Slovenia

Abstract

The present study deals with the numerical analysis of the water droplet evaporation in the carrier gas inside an Ultrasonic Spray Pyrolysis (USP) device. Droplet evaporation is studied through numerical CFD simulation employing Ansys Fluent version 16.1 software. The governing equations for mass, momentum, and energy contain source terms for the effects of droplet evaporation. The results are provided as time dependent evaporation rate, temperature and diameter of droplet. Additional experimental evaporation of $HAuCl_4$ solution droplets with temperatures of 80, 100 and 120°C was performed on a USP device. The obtained dried particles of gold chloride were characterized with TEM and analysed for their size and shapes in order to determine the effect of evaporation rate on the dried particle morphology. This provides insight into selecting optimal parameters for gold nanoparticle synthesis with $HAuCl_4$ in USP, for targeted sizes and shapes of the nanoparticles.

KEYWORDS: Evaporation, Numerical modelling, Water droplet, Dried particles, TEM characterization

Abbrevation

CFD Computational Fluid Dynamics

USP Ultrasonic Spray Pyrolysis

TEM Transmission Electron Microscopy

1 INTRODUCTION

Ultrasonic Spray Pyrolysis (USP) is an aerosol processing technique used for the synthesis of nanomaterials from different materials in various types of nanostructures and thin films. It can be used to synthesize nanoparticles of metallic, metallic oxides, sulphides, carbons and other materials as dense or porous spherical, triangular, cylindrical, core-shell, ball-in-ball and other types of nanoparticles [1–3].

In principle, USP uses a precursor solution sprayed into aerosol droplets with ultrasound, from which the nanoparticles are produced [4]. An inert carrier gas (such as N_2) then transports the droplets into a reaction furnace. In this furnace, the synthesis stages take place: Droplet evaporation, thermal decomposition, reduction or oxidation (if needed) and densification into final nanoparticles. An important stage for the nanoparticle morphology is the droplet evaporation [5]. As the droplet evaporates, it shrinks and the material inside reaches supersaturation and precipitates. Depending on the rate of evaporation, different conditions for the precipitate are possible [3]. If the evaporation is too fast, a crust is formed around the droplet, as the concentration on the surface of the droplet reaches supersaturation quickly, leaving the rest of the droplet trapped inside. When the evaporation is slow enough, the material inside has time for diffusion into the centre of the droplet and, as the droplet slowly shrinks, the dense sphere of the precipitate

is formed. Different shapes and sizes of nanoparticles can be obtained depending on the evaporation rate. Evaporation and drying is an essential element in many processes for the preparation of nanoparticles [6]

Identifying the processes of formation during USP nanoparticle synthesis is challenging due to the very small dimensions of the materials. For this reason, an analytical approach was chosen, with a numerical analysis of the droplet evaporation. The optimal parameters of the USP device can be selected from this analysis in order to obtain desired nanoparticle shapes. The droplet evaporation and drying conditions are also important for decreasing production costs and increasing product yield [7,8]

In addition, droplet evaporation was also performed experimentally with USP. A solution with $HAuCl_4$ dissolved in water was used, aerosolized and transported through a heated tube furnace at temperatures for evaporation [9]. In this way, the first USP synthesis stage of droplet evaporation was simulated for the synthesis of gold nanoparticles. The small particles of the dried aerosol collected in the experiment represent an intermediate product in the USP process for gold nanoparticle synthesis.

While the on-site experimental testing provides the most direct assessment of the precursor droplets` evaporation process, often the cost and availability of testing is limited or even impossible. Obtaining the required resources and trained personnel or training staff for performing the experiments is also challenging. Therefore, the development of computer-aided process design of drying, such as Computational Fluid

Dynamics (CFD) has become very useful for this type of application [8]. However, the numerical modelling of the discrete phase and prediction of the final product properties in USP is a challenging task due to rapid evaporation, varying drying histories of each droplet and limited access for experimental measurements. Furthermore, a number of functionalities of the final product (nanoparticles, powders, etc.) obtained after spray drying are affected by the temperature and moisture content histories that precursor droplets experience inside the dryer [10]. For that, it is customary to start with the Single Droplet Drying (SDD) approach [11,12]. There are several models for Single Droplet drying with two-component systems, such as glucose/water [13], lactose/water [14,15], dissolved solids (sodium sulphate, calcium chloride, sodium acetate, etc. [16]), and others, while models specifically for aqueous gold chloride do not exist. Based on already known similar models [17], we have tried to verify our numerical model in connection with our experiments with droplet drying and TEM microscopy.

The objective of the present study is therefore to investigate the evaporation process of the water droplet in the pilot USP device numerically. For this we have used the Euler-Lagrange approach, where the conservation equations of the continuous gaseous phase were solved and coupled with the discrete water droplet phase.

2 NUMERICAL METHOD

The simulation performed involves the evaporation of a single water droplet in the carrier gas (nitrogen) flow. The numerical modelling of the phenomenon was carried out by adopting a Eulerian-Lagrangian approach. In this approach the Lagrangian phase (water)

moves within a continuous Eulerian phase (nitrogen). We made the following assumptions to simplify the analysis:

- A spherical water droplet ($Ca = \frac{\eta v}{\sigma} \ll 1$) is considered with a uniform temperature ($Bi = h\frac{L_c}{k} \ll 1$).
- Pure component liquid droplet in a carrier gas environment with little solubility of gas in a liquid.

The liquid/gas interface is, at local equilibrium, saturated with vapour at the droplet temperature.

Heat conduction is the mechanism of heat transfer within the droplet.

Nitrogen-water vapour mixture obeys the ideal gas flow

- The gas flow over the droplet is laminar ($Re = \frac{\rho \bar{v} D}{\eta} < 2300$), leading to an average drag force, average heat and mass transfer coefficients, which can all be correlated with the corresponding Reynolds number and properties of the vapour and gas mixture. In other words, no attempt was made to consider detailed flow, heat and mass transport within the droplet.

Radiation heat transfer is neglected.

2.1 Continuous Phase

The continuous (i.e. gas) phase was modelled as laminar flow an ideal gas mixture of nitrogen (carrier gas) and evaporated water vapour. For both mixture species, the temperature dependent physical properties were accounted for [18].

The final result is the familiar form for of the continuity, momentum and energy equations together with the transport equation for species [19]:

$$\frac{\partial \rho}{\partial t} + \frac{\partial\ \rho v_j}{\partial x_j} = S_m \tag{1}$$

$$\frac{\partial\ \rho v_i}{\partial t} + v_j \frac{\partial\ \rho v_i}{\partial x_j} = -\frac{\partial p}{\partial x_i} + \frac{\partial \tau_{ji}}{\partial x_j} + \rho g_{i+} S_P \tag{2}$$

$$\frac{\partial\ \rho c_t T}{\partial t} + v_j \frac{\partial\ \rho c_p T}{\partial x_j} = k \frac{\partial^2 T}{\partial x_j x_j} + S_T \tag{3}$$

$$\frac{\partial C_n}{\partial t} + v_j \frac{\partial\ C_n}{\partial x_j} = \frac{\partial}{\partial x_j}\left(D \frac{\partial C_n}{\partial x_j} \right) + S_n \tag{4}$$

The first and second terms in Eq. (1) to (4) are accumulation and advection of the conserved property respectively. In the above equations, S_m, S_P, S_T and S_n are source terms, due to the presence of particles, for mass, momentum, energy and concentration respectively.

2.2 Discrete Phase

The trajectory of a discrete phase is determined by integrating the force balance on the droplet, which is written in a Lagrangian reference frame. This force balance equates the droplet inertia with the drag force acting on the droplet, and can be written as [19]:

$$\frac{d\vec{v}_p}{dt} = F_D\ \vec{v} - \vec{v}_p\ + \frac{\vec{g}\ \ \rho_p - \rho}{\rho_p} \tag{5}$$

where $F_D\ \vec{v} - \vec{v}_p$ is the drag force per unit droplet mass

$$F_D = \frac{18\eta}{\rho_p d_p^2}\frac{C_D Re}{24} \tag{6}$$

Here, $\vec{v}$ is the fluid phase velocity, $\vec{v}_p$ is the discrete phase velocity, η is the dynamic viscosity of the fluid, ρ is the fluid density, ρ_p is the density of the discrete phase, and d_p is the droplet diameter. Re is the relative Reynolds number

$$Re = \frac{\rho d_p \left|\vec{v}_p - \vec{v}\right|}{\eta} \tag{7}$$

and $C_D = a_1 + a_2 / Re + a_3 / Re^2$ is the drag coefficient for smooth particles [20]. The values of a_1, a_2 and a_3 for different intervals of Reynolds number are listed in Table 1.

The heat and mass transfer between gas phase and droplet takes place at the interface of the droplet and the surrounding gas. Whenever a water droplet is in contact with a gas stream, a film of saturated gas-vapour is formed on the droplet surface. Heat transfer takes place if a temperature difference exists between the liquid temperature at the surface and the gas dry-bulb temperature. Additionally, mass transfer takes place if a vapour concentration gradient exists between the vapour layer and the ambient gas.

The heat balance relating the sensible heat change in the droplet to the convective heat transfer between the droplet and the gas phase is [19]:

$$m_p c_p \frac{dT_p}{dt} = hA_p \left(T_\infty - T_p\right) - \frac{dm_p}{dt} h_{fg} \tag{8}$$

where m_p is the mass of the droplet, c_p is the heat capacity of the droplet, T_p is the droplet temperature, A_P is the surface area of the droplet, T_∞ is the local temperature of the gas phase, h_{fg} is the latent heat, and h is the convection heat transfer coefficient, which is obtained by the empirical correlation of [21]

$$Nu = \frac{hd_p}{k_{fg}} = 2.0 + 0.6 Re^{1/2} Pr^{1/3} \tag{9}$$

where the Prandtl number $Pr = \frac{\eta c_p}{k}$ refers to the continuous (gas) phase.

For high evaporation rates, the effect of convective flow of the evaporating material from the droplet surface to the bulk phase (Stefan flow) becomes important. For that, the mass transfer (mass loss) of the droplet due to evaporation is calculated by the Spalding evaporation model [22,23]

$$\frac{dm_p}{dt} = k_c A_p \rho_\infty \ln\left(1 + B_m\right) \tag{10}$$

where $k_c = Sh \frac{D_{i,m}}{d_p}$ is the mass transfer coefficient (determined from the Sherwood number $Sh = 2.0 + 0.6 Re^{1/2} Sc^{1/3}$), A_P surface area of the droplet, ρ_∞ is the density of the bulk phase. B_m is the Spalding mass number given by

$$B_m = \frac{Y_{i,s} - Y_{i,\infty}}{1 - Y_{i,s}} \tag{11}$$

where $Y_{i,s}$ and $Y_{i,\infty}$ are the vapour mass fractions at the surface and in the bulk phase. In the limit of small B_m, $ln\ 1+B_m \approx B_m$ and the Spalding model reduces to the gradient diffusion model.

2.3 Geometry And Boundary Conditions

The problem of the droplet evaporation in a hydrodynamically and thermally developed carrier gas flow is depicted schematically in Fig. 1. The tubular furnace was a quartz tube with an inside diameter of $21mm$ and length of $700mm$. Nitrogen, as the carrier gas, was kept at a flow rate of $1.5l/min$. For the present study, the tubular furnace was kept at two heating temperatures of $80℃$ and $100℃$.

The inlet to the flow domain is located some distance upstream from the heated furnace (this is taken as the coordinate origin, $x = 0$), while the outlet is located far downstream from the heated furnace. The steady velocity profile and fixed temperature were imposed at the inflow boundary. At the outflow boundary we imposed the zero diffusion flux for all flow variables; this means that the conditions were extrapolated from within the domain and had no impact on the upstream flow. The wall boundary conditions represented the surface of the heated (L_2) and unheated (L_1, L_3) tube walls:

- Unheated tube wall – natural convection from the horizontal cylinder [24])

$$q = h_{ext}\ \left(T_{\infty} - T_{Wall}\right)$$

$$h_{ext} = Nu\,\frac{k}{D} \tag{12}$$

$$Nu = \left[0.6 + \frac{0.387 Ra^{1/6}}{\left[1 + \left(0.559/Pr\right)^{9/16}\right]^{8/27}}\right]^2$$

- Heated tube wall – experimentally determined wall temperature (Fig. 2)

Finally, the water droplet of initial diameter $5\mu m$ and temperature $296.15K$ was injected at $x = 0,\ y = 0,\ z = 0$ with the zero relative (according to the gas phase) velocity.

3 GRID REFINEMENT AND NUMERICAL ACCURACY ASSESSMENT

The grid independence of the present results has been established on the basis of a detailed analysis using four different meshes (the elements were concentrated towards each solid wall). With each grid refinement the number of elements in a particular direction is increased and the element size is reduced. Such a procedure is useful (and encountered in many numerical studies [25–27]) for applying the Richardson's extrapolation technique, which is a method for obtaining a higher-order estimate of the flow value from a series of lower-order discrete values.

For a general variable ϕ the grid-converged value according to the Richardson extrapolation is given as:

$$\phi_{ext} = \phi_{MII} - \left(\phi_{MII} - \phi_{MIII}\right) / \left(r^{p} - 1\right) \tag{12}$$

where ϕ_{MIII} is obtained on the finest grid and ϕ_{MII} is the solution based on the next level coarse grid, $r = 1.5$ is the ratio between coarse to fine grid spacing and $p = 2$ is the order of accuracy.

The variation of liquid fraction and temperature with grid refinement is given in tabulated form in Table 2. The "percent" numerical error as given in Table 2 is a quantification of the relative difference between the numerical predictions and the extrapolated value obtained with Richardson's extrapolation technique.

The results of numerical accuracy analysis indicate that, as the mesh is refined, there is a consistent improvement in the accuracy of the predicted values, and the agreement between predictions obtained with mesh MII and the extrapolated value is extremely good. Based on this, the simulations in the remainder of the paper were conducted on mesh MII, which provided a reasonable compromise between high accuracy and computational effort.

4 MODEL VERIFICATION

There is a lack of validation cases for evaporation of droplets having diameters less than $50\mu m$. For that, the present study has been validated by studying the evaporation of a single water droplet (initial diameter: $200\mu m$, initial temperature: $50℃$) suspended in still humid air (relative humidity: 20%, temperature: $50℃$). Comparison of present results with the results of Alroe [28] shows that the present CFD model captured the

evaporation of the single droplet correctly, thereby verifying our modelling approach (Fig. 3).

5 EXPERIMENTAL METHOD

A precursor solution of $HAuCl_4$ diluted with water was prepared, with a concentration of 2.5g/l of Au. An ultrasonic nebulizer Gapusol RBI 9000 (France) with an ultrasound frequency of 2.5MHz was used to produce aerosol droplets of the precursor solution. Nitrogen gas was introduced into the nebulizer at flow rate of 1.5l/min for transporting the aerosol into the quartz tube (inside diameter of 21mm). The quartz tube was positioned inside a tubular furnace (28 cm length), which was kept at two heating temperatures of 80℃ and 100℃. At the end of the tubular furnace, a SiN TEM grid was positioned vertically, for deposition of dried particles intended for TEM analysis (Fig. 4). The deposition time was 1.5 hours for both evaporation experiments.

Conventional Transmission Electron Microscopy (TEM; JEOL 2100) investigations were conducted on the samples prepared in the experiments. The dried particles size distributions measurements and shape determination was done with ImageJ software [29], from 10 TEM micrographs of each sample. The number of dried particles for size distributions ranged from 300 to 600 per micrograph. Measurements were carried out based on the procedures in [30].

After analysis of the dried aerosol particles, it was determined, that a third experiment (heating temperature of 120°C) was needed for determining the trend for aerosol drying in terms of shapes and sizes of the obtained dried particles at different evaporation rates.

6 RESULTS AND DISCUSSION

6.1 Carrier Gas Flow

The temperature variations along the tube axis as determined from the numerical simulation are illustrated in Fig. 5.

The temperature distributions for the two temperature settings of the furnace ($80℃,100℃$) did not appear to be symmetrical along the vertical centreline of the heated furnace (as one would expect for the case of zero nitrogen velocity) due to the effect of the carrier gas flow. The maximum temperature is shifted towards the exit of the heated furnace. Furthermore, one can expect that the increased velocity (volume flow) of carrier gas would result in a further shift of the temperature maximum.

Fig. 6 shows temperature distributions on the vertical mid-plane of the heated tube. The temperature of the upper wall of the tube is higher than that of the bottom wall. As the carrier gas passes through the heated zone and its temperature is increased, its velocity vector gains an upward component due to the effect of buoyancy. Accordingly, hotter carrier gas exhibits motion in the upward direction (Fig. 7) associated with its motion in the axial direction (Fig. 8). Furthermore, the hotter the carrier gas is, the greater is the magnitude of vertical velocity.

With respect to the temperature distributions obtained for each heating temperature (Fig. 6), the lowest temperature gradient is produced by the lowest heating rate, and consequently, the slower evaporation rate of the liquid phase can be expected. On the other hand, higher temperature regimes could cause faster heating and cooling, with steeper temperature gradients associated with the introduction of higher energy for droplet evaporation as well as for the growth and agglomeration of primary particles.

6.2 Droplet Evaporation

During a certain (but relatively short) transient time, the drop cools down due to evaporation until it reaches its wet-bulb temperature, the value of which depends on the ambient temperature and relative humidity (Fig. 9). At the same time, a thin layer of saturated vapour is formed around the drop. Since the temperature of the drop is lower than that of the carrier gas, heat flows towards the drop and "feeds" the evaporation process. When the drop is at its stable wet-bulb temperature it continues to shrink due to "steady" evaporation. The adjective "steady" is used merely to distinguish the evaporation process from the initial cooling-down period; physically evaporation is not a steady process, since the drop shrinks continuously and the evaporation rate changes correspondingly.

The evaporation as predicted by the present study is presented in Fig. 10. Since the droplet was injected with zero relative (to the carrier gas) velocity, its Reynolds number

is $Re \approx 0$ and the evaporation is diffusion controlled. Due to that, the rate of change of the square of the droplet diameter is constant and follows the so-called D^2 law.

6.3 Experimental Deposition Of Dried Particles

While there are theoretical models available for a number of Single Droplet Drying systems, experimental measurements are still needed for validation of theoretical investigations [16], for realistic predictions of the obtained gold particle morphology and practical recommendations in our system with gold chloride. TEM images of the obtained dried aerosol show spherical and polygonal shapes (triangular, trapezoidal, pentagonal and hexagonal) of the gold chloride particles. The most numerous particle shape is spherical, followed by hexagonal shapes of the particles (Table 3).

For evaporation temperature of 80°C, an average particle size of 88.2 nm with a standard deviation of ± 43.3 nm was measured from TEM images. For 100°C, the average size was around 36.2 ± 21.1 nm, while for 120°C it was 27.1 ± 7.4 nm (Fig. 11).

TEM images show no porous, shrivelled or destroyed particles as seen in similar drying experiments [14–16], only solid particles of different shapes. There seems to be no crust of the dissolved chloride forming during drying [14,16], which would yield the previously mentioned particle morphology. This indicates a steady evaporation, where the dissolved chloride moves toward the droplet centre during drying. Even though our simulation involves the evaporation of a single water droplet in a nitrogen gas flow, there is an agreeable similarity between the simulated evaporation and the experimental one. Due to

the low gold chloride concentration (2.5g of gold chloride per 1000g of water), the physical properties of density, viscosity, surface tension, etc., between the water droplet and gold chloride droplet do not differ by much. The simulation model can, therefore, be used for designing and selecting optimal parameters in the USP system (USP dimensions, gas flows, evaporation temperatures) with low gold chloride concentrations.

When comparing droplet drying at 80°C and 100°C, we can see a large difference in size and size distribution of the dried particles. This is not so apparent between 100°C and 120°C (Fig. 11). At 80°C the temperature gradients, evaporation rates and lower velocities (v_y velocity in Fig. 7) give the droplets a longer lifetime and a larger possibility of collisions and coalescence, as compared to 100°C, where the droplets were more dispersed across the tube volume. It seems that there is a threshold between evaporation temperatures of 80 and 100°C for the given gold chloride concentration, where the size distribution of the dried particles becomes much narrower.

As the temperature of evaporation increases more spherical particles are obtained with aerosol drying. It seems a faster evaporation rate favours the formation of more spherical particles. The sizes of the dried particles also decrease with increasing evaporation temperature, while their size distribution becomes narrower. This provides good information about gold nanoparticle synthesis in a USP with a separate evaporation for obtaining the desired shapes and sizes of gold nanoparticles. In order to obtain small spherical particles of a few 10 nm in size, the evaporation should be fast enough to prevent the formation of other shapes and larger sizes. To obtain other shapes and sizes

with high uniformity with USP presents a more complex problem, where a higher control of the evaporation stage is needed. For this purpose, the USP process and construction elements need to be more refined, with a more precise aerosol generator, capable of generating droplets in a narrow size distribution, with improved and very accurate heating systems and optimal transport tube dimensions, based on further advancing the numerical work carried out in this article.

As the droplet diameters reach very small sizes during evaporation and drying (a few 10 nm), the flow regime is in a transition stage where the continuum assumption is not accurate [5]. As such, non-continuum effects should also be taken into account for further numerical work. However, the numerical analysis done here shows a good model of the flow regimes and evaporation rates in our existing USP equipment. This gives us the information required for optimising the process parameters and producing nanoparticles with desired characteristics of shape and size.

7 CONCLUSIONS

The present work deals with numerical modelling of water droplet evaporation in the flow of a carrier gas (N_2) in the 1st stage of an Ultrasonic Spray Pyrolysis device. For that we have employed the Euler-Lagrange approach, where the gas phase is treated as continuum, while the water droplet is treated as a discrete particle.

The influence of computational grid refinement on the present numerical predictions was studied throughout the examination of spatial (grid) convergence for the flow of carrier

gas. In addition, Richardson's extrapolation technique was used to quantify the numerical accuracy for the axial velocity and temperature at the centre of the tubular furnace (error levels are below 0.60%).

The numerical model was validated for the case of single droplet evaporation in surrounding stationary humid air for which the results are available in the open literature. Remarkable agreement of present results with the available results yields sufficient confidence in the present numerical procedure and results.

For the case of the water droplet evaporation in the carrier gas, the following important conclusions are pointed out:

- As the carrier gas passes through the heated zone and its temperature is increased, its velocity vector gains an upward component due to the effect of buoyancy. Accordingly, hotter carrier gas exhibits motion in the upward direction associated with its motion in the axial direction.
- The lowest temperature gradient is produced by the lowest heating rate, and consequently, the slower evaporation rate of the liquid phase can be expected. On the other hand, higher temperature regimes could cause faster heating and cooling, with steeper temperature gradients associated with the introduction of higher energy for droplet evaporation as well as for the growth and agglomeration of primary particles.
- Since the droplet was injected with zero relative (to the carrier gas) velocity, its Reynolds number is $Re \approx 0$ and the evaporation is diffusion controlled. Due to that, the

rate of change of the square of the droplet diameter is constant and follows the so-called D^2 law.

The simulation involves evaporation of a single water droplet, while droplets with dissolved gold chloride are used for the experimental part. The absence of hollow, porous or destroyed particles indicate no crust formation and a steady drying with the gold chloride moving towards the centre of the droplet during evaporation. The numerical simulation can, therefore, be used in selecting optimal parameters in a USP system with low gold chloride concentrations. The evaporation temperature and resulting evaporation rate influences the shape, size and size distribution of the obtained dried particles:

- Lower temperatures yield large dried particles in a broad size distribution of various shapes. Higher temperatures yield smaller dried particles in a narrower size distribution and a greater number of spherically shaped dried particles.

ACKNOWLEDGEMENTS

The research was carried out under the Young Researcher Program funded by the Slovenian Research Agency (ARRS) and the Research Program P2-0120. We would like to thank Dr. Darja Jenko of the IMT Institute of Metals and Technology, Ljubljana for carrying out the TEM investigations.

APPENDIX A: PHYSICAL PROPERTIES

This section gives data and information on the calculation approach for physical properties of the different gases and liquid used in this study.

Gas phase properties [7]

$$c_p = R\left\{B + C - B\left(\frac{T}{A+T}\right)^2\left[1-\left(\frac{A}{A+T}\right)\left(D+E\left(\frac{T}{A+T}\right)\right.\right.\right.$$
$$\left.\left.\left.F\left(\frac{T}{A+T}\right)^2+G\left(\frac{T}{A+T}\right)^3\right)\right]\right. \quad \text{(A1)}$$

	Nitrogen	Air	Water vapour
R [$J/kg\ K$]	296.8039	287.12	461.526
A [/]	432.2027	2548.9320	706.3032
B [/]	3.5160	3.5248	5.1703
C [/]	2.8021	-0.6366	-6.0865
D [/]	-4.1924	-3.4281	-6.6011
E [/]	42.0153	49.8238	36.2723
F [/]	-114.2500	-120.3466	-63.0965
G [/]	111.1019	98.8658	46.2085

$$k = A + BT + CT^2 + DT^3 + ET^4 \quad \text{(A2)}$$

	Nitrogen	Air	Water vapor
A [/]	-1.330E-04	-9.080E-04	13.918E-03
B [/]	1.010E-04	1.120E-04	-4.700E-05
C [/]	-6.065E-08	-8.4333E-08	2.58066E-07
D [/]	3.361E-11	5.6964E-11	-1.83149E-10
E [/]	-7.100E-15	-1.5631E-14	5.5092E-14

$$\eta = A + BT + CT^2 + DT^3 + ET^4 \quad \text{(A3)}$$

	Nitrogen	Air	Water vapor
A [/]	-1.020E-07	-1.702E-07	6.4966E-06
B [/]	7.4785E-08	7.9965E-08	-1.5102E-08
C [/]	-5.9037E-11	-7.2183E-11	1.15935E-10
D [/]	3.230E-14	4.960E-14	1.008E-13
E [/]	-6.730E-18	-1.388E-17	3.100E-17

GASEOUS MIXTURE PROPERTIES

The gaseous mixture properties were calculated using the inbuilt mixing law and kinetic theory based formulations in ANSYS Fluent.

Density	Ideal incompressible gas
Thermal conductivity	Ideal gas mixing law
Specific heat capacity	Ideal gas mixing law
Viscosity	Ideal gas mixing law
Mass diffusivity	Kinetic theory

Water droplet properties [7]

$$\rho = \rho_{cr} + A\left(1-\frac{T}{T_{cr}}\right)^{0.35} + B\left(1-\frac{T}{T_{cr}}\right)^{2/3} + C\left(1-\frac{T}{T_{cr}}\right) + D\left(1-\frac{T}{T_{cr}}\right)^{4/3} \quad \text{(A4)}$$

$\rho_{cr}\left[kg/m^3\right]$	T_{cr} K	*A* [/]	*B* [/]	*C* [/]	*D* [/]

322	647.096	1094.023	-1813.23	3863.956	-2479.81

$$c_p = R\left[\left(\frac{A}{1-T/T_{cr}}\right)+B+C\left(1-\frac{T}{T_{cr}}\right)+D\left(1-\frac{T}{T_{cr}}\right)^2+E\left(1-\frac{T}{T_{cr}}\right)^3 + F\left(1-\frac{T}{T_{cr}}\right)^4\right] \quad \text{(A5)}$$

R [*J/kg K*]	461.526
T_{cr} *K*	647.096
A [/]	0.2399
B [/]	12.8647
C [/]	-33.6392
D [/]	104.7686
E [/]	-155.4709
F [/]	92.3726

$$h_{fg} = RT_{cr}\left[A\left(1-\frac{T}{T_{cr}}\right)^{1/3}+B\left(1-\frac{T}{T_{cr}}\right)^{2/3}+C\left(1-\frac{T}{T_{cr}}\right)+D\left(1-\frac{T}{T_{cr}}\right)^2 + E\left(1-\frac{T}{T_{cr}}\right)^6\right] \quad \text{(A6)}$$

R [*J/kg K*]	461.526
T_{cr} *K*	647.096

A [/]	6.85307
B [/]	7.43804
C [/]	-2.937595
D [/]	-3.282093
E [/]	8.397378

$$ln\frac{p_s}{p_{cr}}=\frac{T_{cr}}{T}\left[A\left(1-\frac{T}{T_{cr}}\right)+B\left(1-\frac{T}{T_{cr}}\right)^{1.5}+C\left(1-\frac{T}{T_{cr}}\right)^{2.5}+D\left(1-\frac{T}{T_{cr}}\right)^{5}\right] \quad \text{(A7)}$$

p_{cr} Pa	2.2064E+07
T_{cr} K	647.096
A [/]	-7.86975
B [/]	1.90561
C [/]	-2.30891
D [/]	-2.06472

$$D_{H_20-N_2}=21.9E-06\left(\frac{T}{273.15}\right)^2 \quad \text{(A7)}$$

$$D_{H_20-air}=A+BT+CT^2 \quad \text{(A8)}$$

A [/]	-2.775E-06
B [/]	4.479E-08

C [/]	1.656E-10

REFERENCES

[1] Milosevic, O. B.; Mancic, L.; Rabanal, M. E.; Gomez, L. S.; Marinkovic, K. Aerosol route in Processing of Nanostructured Functional Materials. KONA Powder and Particle Journal **2009**, 27 (0), 84–106.

[2] Messing, G. L.; Zhang, S.-C.; Jayanthi, G. V. Ceramic Powder Synthesis by Spray Pyrolysis. Journal of the American Ceramical Society **1993**, 76 (11), 2707–2726.

[3] Kodas, T. T.; Hampden-Smith, M. J. Aerosol Processing of Materials, 1 edition; Wiley-VCH: New York, **1998**.

[4] Deguchi, S.; Matsuda, H.; Hasatani, M.; Kobayashi, N. Formation mechanism of TiO2 fine particles prepared by the spray pyrolysis method. Drying Technology **1994**, 12 (3), 577–591.

[5] Jayanthi, G. V.; Zhang, S. C.; Messing, G. L. Modeling of Solid Particle Formation During Solution Aerosol Thermolysis: The Evaporation Stage. Aerosol Science and Technology **1993**, 19 (4), 478–490.

[6] Wang, B.; Zhang, W.; Zhang, W.; Mujumdar, A. S.; Huang, L. Progress in Drying Technology for Nanomaterials. Drying Technology **2005**, 23, 7–32.

[7] Dufour, P. Control Engineering in Drying Technology: Review and Trends. Drying Technology **2006**, 24, 889–904.

[8] Strumiłło, C. Perspectives on Developments in Drying. Drying Technology **2006**, 24, 1059–1068.

[9] Majerič, P.; Friedrich, B.; Rudolf, R. Au-nanoparticle synthesis via ultrasonic spray pyrolysis with a separate evaporation zone. Materials and Technology **2015**, 49 (5), 791–796.

[10] Fu, N.; Woo, M.W.; Chen, X.D. Single droplet drying technique to study drying kinetics measurement and particle functionality: a review. Drying Technology **2012**, 30(15), 1771-1785

[11] Tran, T.T.H.; Jaskulski, M.; Avila-Acevedo, J.G.; Tsotsas, E. Model parameters for single droplet drying of skim milk and its constituents at moderate and elevated temperatures. Drying Technology **2016**, doi:10.1080/07373937.2016.1182548

[12] Fu, N.; Wu, W.D.; Yu, M.; Moo, F.T.; Woo, M.W.; Selomulya, C.; Chen, X.D. In situ observation on particle formation process via single droplet drying apparatus: effects of precursor composition on particle morphology. Drying Technology **2016**, 34(14), 1700-1708

[13] Che, L.; Li, D.; Chen, X.D. Convective drying kinetics of single droplets of aqueous glucose. Drying Technology **2012**, 30(10), 1029-1036.

[14] Tran, T.T.H.; Avila-Acevedo, J.G.; Tsotsas, E. Enhanced methods for experimental investigation of single droplet drying kinetics and application to lactose/water. Drying Technology **2016**, 34(10), 1185-1195.

[15] Chen, X.D. Heat-mass transfer and structure formation during drying of single food droplets. Drying Technology **2010**, 22(1-2), 179-190.

[16] Mezhericher, M.; Levy, A.; Borde, I. Theoretical models of single droplet drying kinetics: a review. Drying Technology **2010**, 28(2), 278-293.

[17] Xiao, J.; Chen, L.; Wu, W.D.; Chen, X.D. Multiscale modeling for nanoscale surface composition of spray-dried powders: the effect of initial droplet size. Drying Technology **2016**, 34 (9), 1063-1072.

[18] VDI Ed. VDI Heat Atlas; Springer: Berlin, Heidelberg, **2010**.

[19] ANSYS Fluent Theory Guide; ANSYS, Inc, USA, **2010**.

[20] Morsi, S. A.; Alexander, A. J. An investigation of particle trajectories in two-phase flow systems. Journal of Fluid Mechanics **1972**, 55 (2), 193-208.

[21] Ranz, W. E.; Marshall, W. R. Evaporation from drops, part I. Chemical Engineering Progress **1952**, 48 (3), 141–146.

[22] Miller, R. S.; Harstad, K.; Bellan, J. Evaluation of equilibrium and non-equilibrium evaporation models for many-droplet gas-liquid flow simulations. International Journal of Multiphase Flow **1998**, 24 (6), 1025–1055.

[23] Sazhin, S. S. Advanced models of fuel droplet heating and evaporation. Progress in Energy and Combustion Science **2006**, 32 (2), 162–214.

[24] Churchill, S.W.; Chu, H.H.S. Correlating Equations for laminar and Turbulent Free Convection from a Vertical Plate. Heat and Mass transfer **1975**, 18, 1049–1053 and 1323-1329..

[25] Bilus, I.; Morgut, M.; Nobile, E. Simulation of Sheet and Cloud Cavitation with Homogenous Transport Models. International Journal of Simulation Modelling **2013**, 12 (2), 94–106.

[26] Ternik, P.; Buchmeister, J. Buoyancy-Induced Flow and Heat Transfer of Power Law Fluids in a Side Heated Square Cavity. International Journal of Simulation Modelling **2015**, 14 (2), 238–249.

[27] Ternik, P.; Rudolf, R. Numerical Analysis of Continuous Casting of NiTi Shape Memory Alloy. International Journal of Simulation Modelling **2016**, 15 (3), 522-531.

[28] Alroe, J. Modelling the Evaporation of a Liquid Droplet. **2014** [Online]. Available: http://vrs.amsi.org.au/wp-content/uploads/sites/6/2014/09/ALROE_Joel._Research_Paper_revised.pdf. [Accessed: 28-Jul-2016].

[29] Schneider, C. A.; Rasband, W. S.; Eliceiri, K. W. NIH Image to ImageJ: 25 years of image analysis. Nature Methods **2012**, 9 (7), 671–675.

[30] Woehrle, G. H.; Hutchinson, J. E.; Özkar, S.; Finke, R. G. Analysis of nanoparticle transmission electron microscopy data using a public-domain image-processing program, image J. Turkish Journal of Chemistry **2006**, 30 (1), 1–13.

Table 1 Constants for different intervals of the Reynolds number for the Morsi-Alexander drag model.

Reynolds number interval	a_1	a_2	a_3
$0 < Re \leq 0.1$	0	24	0
$0.1 < Re \leq 1$	3.690	22.73	0.0903
$1 < Re \leq 10$	1.222	29.1667	-3.8889
$10 < Re \leq 100$	0.6167	46.50	-116.67
$100 < Re \leq 1000$	0.3644	98.33	-2778
$1000 < Re \leq 5000$	0.357	148.62	-47500
$5000 < Re \leq 10000$	0.46	-490.546	578700
$Re > 10000$	0.5191	-1662.5	5416700

Table 2 Effect of mesh refinement upon the axial velocity and temperature at the centre of the tubular furnace ($x = 0.14m,\ y = 0.0m,\ z = 0.0m$) for a steady-state numerical analysis of nitrogen flow.

	MI	MII	MIII	ϕ_{ext}	*Error*
Num. el.	107520	362880	1224720	/	/
$v_x \ \ m/s$	0.1287	0.1278	0.1274	0.1271	0.56%
$T \ \ K$	358.27	358.09	358.01	357.95	0.04%

Table 3 Number percentage of dried particle shapes, obtained from aerosol with $HAuCl_4$

Evaporation temperature	Spherical	Hexagonal	Pentagonal	Trapezoid	Triangular
80°C	38,8%	30,1%	6,8%	10,7%	13,6%
100°C	45,6%	25,3%	3,8%	7,6%	17,7%
120°C	56,8%	12,7%	7,6%	11,0%	11,9%

Figure 1. Schematic representation of geometry.

$L_1 = 0.10m, L_2 = 0.28m, L_3 = 0.32m, D = 0.021m.$

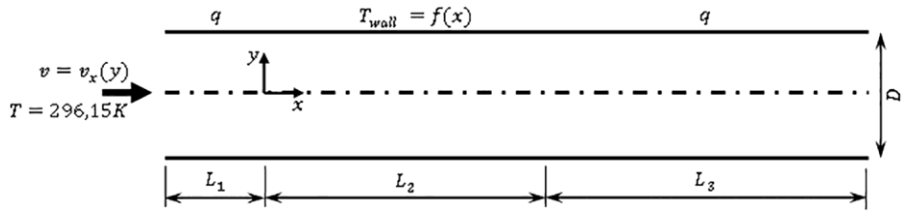

Figure 2. Profiles of tube wall for heating temperatures of $80℃$ and $100℃$.

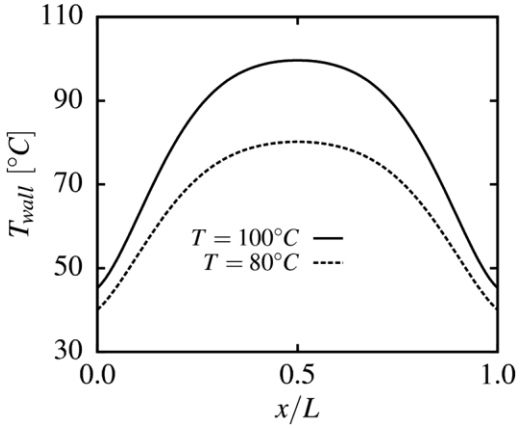

Figure 3. Comparison of the droplet diameter reduction between the present results and the results of Alroe [28].

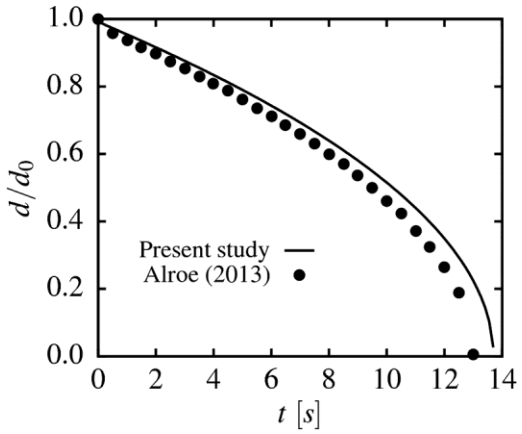

Figure 4. Schematic representation of the USP device used for aerosol drying and dried particle collection

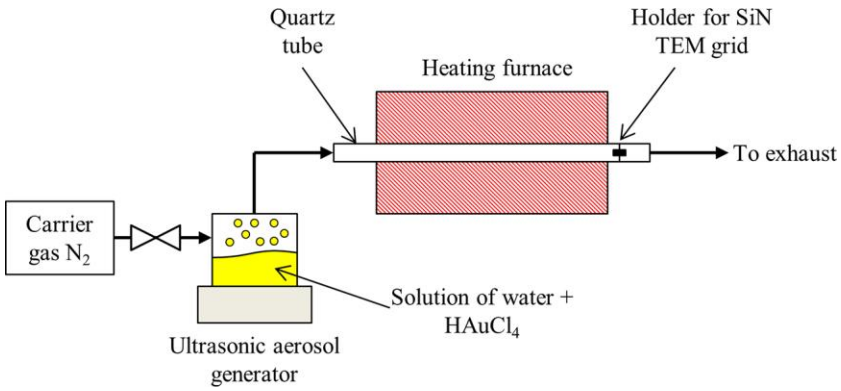

Figure 5. Variation of temperature along the centreline for heating temperatures of $80℃$ and $100℃$.

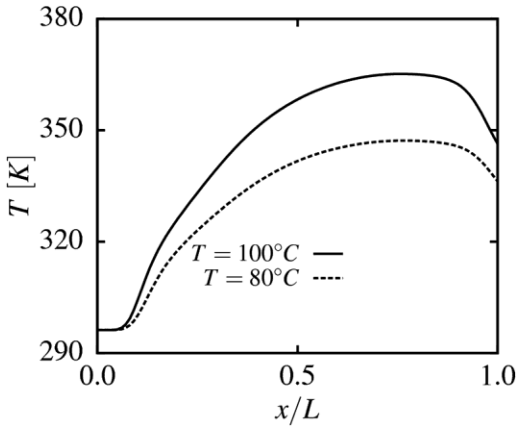

Figure 6. Temperature distributions on a vertical mid-plane $z = 0.0$ for heating temperatures of $80℃$ (top) and $100℃$ (bottom).

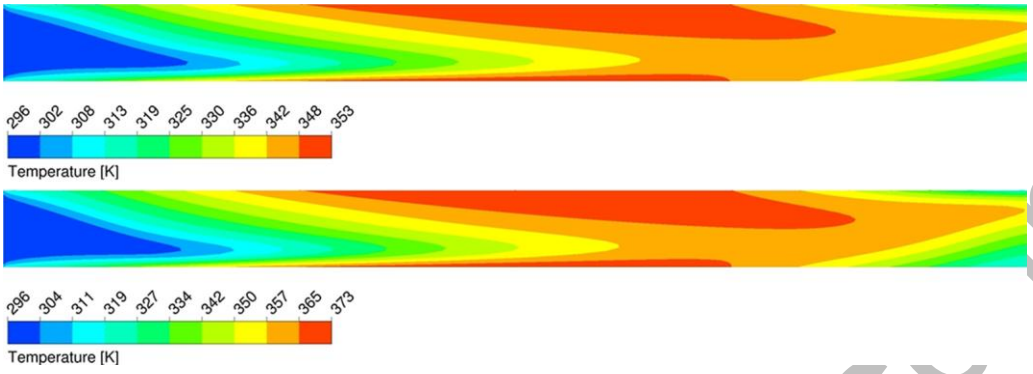

Figure 7. v_y velocity distributions on a vertical mid-plane $z = 0.0$ for heating temperatures of $80℃$ (top) and $100℃$ (bottom).

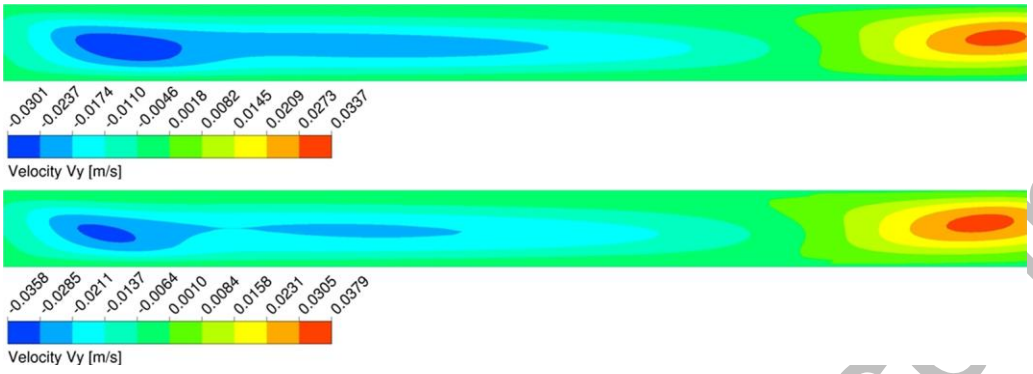

Figure 8. v_x velocity distributions on a vertical mid-plane $z = 0.0$ for heating temperatures of $80℃$ (top) and $100℃$ (bottom).

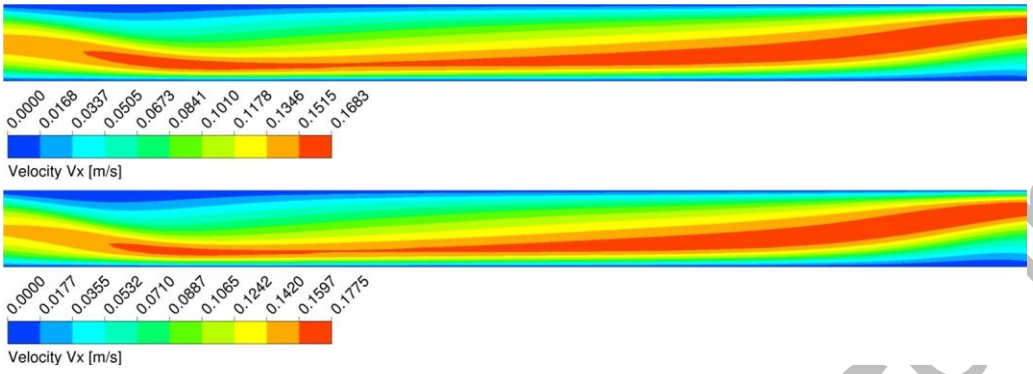

Figure 9. Variation of droplet's surface temperature with time for heating temperature of 100℃.

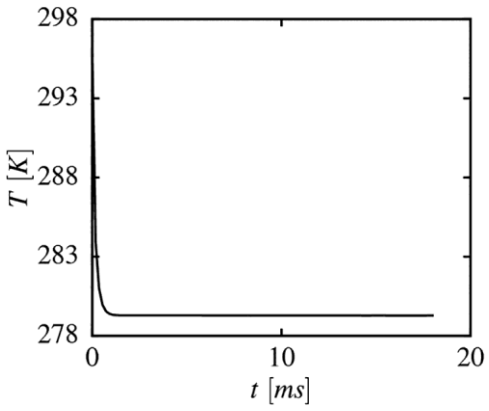

Figure 10. Decrease of drop diameter with time for heating temperature of 100℃.

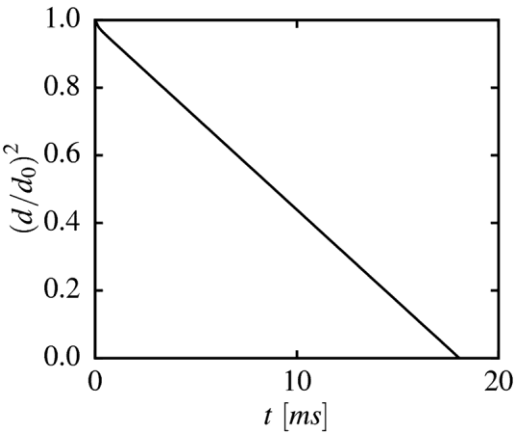

Figure 11. Representative TEM micrograph of obtained dried particles from aerosol, with accompanying histograms of particle size distributions with drying temperatures of 80°C, 100°C and 120°C.